metals

MDPI

Article

A Study of Sliver in C-Shaped Grain Selectors during Investment Casting of Single-Crystal Superalloy

Qiang Yang [1], Xintao Zhu [1,2,*], Fu Wang [1], Dexin Ma [2] and Jiantao Wu [3]

[1] State Key Laboratory for Manufacturing System Engineering, Xi'an Jiaotong University, Xi'an 710049, China
[2] Foundry Institute, RWTH Aachen University, 52072 Aachen, Germany
[3] Central Iron & Steel Research Institute, Beijing 100081, China; 13501190634@139.com
* Correspondence: zhudb8@gmail.com

Abstract: In this study, the formation mechanism of sliver defects in C-shaped 2D grain selectors during investment casting of single-crystal superalloy was investigated by analyzing the effects of the C-shaped 2D grain selectors on the solidification behavior of superalloy. The physical field properties of the sliver formation and solidification characteristics of CM247LC nickel-based superalloy were determined. The temperature and stress fields were simulated using ProCAST. The results showed that the stress fields of solidification played an essential role in the formation of sliver, indicating that the solidification interval characteristics of the alloy and stress based on the geometry of the C-shaped 2D grain selector are crucial for the formation of sliver. In addition, the origin of sliver depended upon tensile stress during solidification, relying on the constraints of dendrite boundaries. The findings suggested that the joint sections of the starter block—i.e., selector and selector-casting joint of C-shaped selector sections—are stress-sensitive areas where sliver can form readily. Furthermore, sliver is formed in the final stages of solidification and especially originates in the grain selection part where the accumulated thermal stress is high, and there is only a small quantity of liquid phase with a low melting point between the dendrites. Therefore, the solidification and stress conditions generate thermal cracks, which can also cause sliver defects.

Keywords: directional solidification; single crystal; sliver; C-shaped grain selector; stress

check for updates

Citation: Yang, Q.; Zhu, X.; Wang, F.; Ma, D.; Wu, J. A Study of Sliver in C-Shaped Grain Selectors during Investment Casting of Single-Crystal Superalloy. *Metals* **2023**, *13*, 1102. https://doi.org/10.3390/met13061102

Academic Editors: Nikki Stanford and Reza Ghomashchi

Received: 14 February 2023
Revised: 23 May 2023
Accepted: 30 May 2023
Published: 12 June 2023

Copyright: © 2023 by the authors. Licensee MDPI, Basel, Switzerland. This article is an open access article distributed under the terms and conditions of the Creative Commons Attribution (CC BY) license (https://creativecommons.org/licenses/by/4.0/).

1. Introduction

Ni-based single-crystal (SX) superalloy is widely used due to its excellent high-temperature performance [1,2]. SX crystallization is vital for improving the turbine blade's initial temperature and creeping resistance at high temperatures. To obtain the single-crystal structure with a superior mechanical property, the design of the grain selector is a crucial factor in the casting process. In the past few years, several kinds of grain selectors (such as the restrictor, as well as the angled and spiral selectors) were designed to achieve a high-efficiency grain selector for growing SX blades [3–5]. However, the application of restrictor selector was limited due to lower efficiency caused by a longer length for selecting a single grain [6]. In order to overcome the shortcomings of traditional selectors, the 2D grain selector was proposed as a candidate to obtain a high-quality single crystal. The C-shaped and Z-shaped 2D grain selectors were proposed, and the effects of geometry of the selector on grain selection were investigated by our research group in previous works [7–9]. However, in recent studies, the sliver defect was found by using the C-shaped grain selectors during investment casting of SX blades. The sliver is a easily neglected defect, which could cause a decrease in the performance of single-crystal blades and the rejection of casting for the mass manufacturing of blades [10,11], when the single-crystal blades were produced via the single-crystal directional solidification process. Therefore, the causes of the sliver defect must be investigated in-depth when the C-shaped grain selectors are applied in investment casting of single-crystal blades.

Over the past several decades, many efforts have focused on the reasons for the sliver defect formation of SX superalloy in the directional solidification process. Beech et al. [12] asserted that the sliver formed due to casting shrinkage. Schaefer [13] argued that the development of sliver was induced by a strong stress acting on dendrites. This stress is considered to be a result of differential thermal contraction, double-diffusive convective flow, coupled vibration mediated coupling, or buoyancy. Aveson et al. [14] systematically investigated the formation of sliver in the "neck channel" between the seed and the root of the turbine blade. Their investigation revealed that the development of the sliver is mainly due to the stress during the solidification on the growth of dendrites, causing the dendrites to deflect, and unrelated to the impurities caused by oxide inclusions, dendritic melting, or the deflection of dendrites in the necking channel. Zhang et al. [15,16] inferred that the cause of the sliver was the deformation of dendrites, and the factors inducing dendritic deformation were mainly related to defects inside the casting, such as inclusions. Liu et al. [17,18] found that the sliver correlated with the stress caused by the structure of the blade. Jiang et al. [19] proposed the viewpoint that the slivers evolved from freckles, specifically when the growth orientation of freckles was consistent with the direction of the temperature gradient. Ma et al. [20] studied the formation mechanism of the sliver and found that its defects originated from the tearing of the existing dendrite stems in the mush zone, revealing a clear starting point of the sliver defect. However, due to the intricate relationship between the sliver formation and dendritic growth morphology, thermosolutal gradients, convection, and strong stress make it difficult to determine the exact reason responsible for the sliver's formation.

When the solid isotherm passes through the necking channel, the stress in the necking channel is distributed asymmetrically. Consequently, dendrite deflection occurs in the necking channel, leading to the formation of the sliver. Therefore, investigating the micro mechanisms of the sliver's formation, especially the dendrite deflection from the necking channel, is significant to understanding how the sliver forms. Although dendrite deflection is thought to be the reason for the formation of the sliver, it is still unclear whether convection can induce dendritic deflection during solidification. Pilling et al. [21] estimated the stress of the interdendritic convection rate on the dendrite at a microscale of 10 mm/s and discovered that it was less than the yield strength. Thus, they concluded that the interdendritic convection would not cause dendritic deflection. Dragnevski et al. [22] reported that dendritic deflection would only occur when the degree of undercooling was between 50 °C and 100 °C, and when the convection rate was 100 mm/s. The convection rate is generally below 100 mm/s, and the degree of undercooling is also less than 50 °C. Therefore, the convection is insufficient to induce dendrite deflection. In order to find out the causes of the sliver defect formation, the effects of C-shaped 2D grain selection on the sliver defect was studied in this paper. Particular attention was paid to the origins of the sliver formation, especially how the solidification originates. We also considered the necking channel of the simplified 2D grain selection.

2. Experimental Procedure

2.1. Test and Calculation Method

2.1.1. Experimental Method

The CM247LC alloy was used as raw material in the experiment; the chemical composition of CM247LC alloy is listed in Table 1. The wax pattern and the cluster of ceramic shell are shown in Figure 1. The thickness of the shell was set as 7–8 mm. The grain selector casting samples were divided into eight groups and labeled from SC_{d1} to SC_{d8}. SCd represents the C-shaped selector sample with varying wire diameters (d_1/2.6 mm–d_8/6.6 mm). To ensure the accuracy of the experiment, a vacuum Bridgman VIM-IC furnace (ALD Vacuum Technologies GmbH, Hanau, Germany) was used for directional solidification experiment. The chill plate had a width of 200 mm, whilst the corresponding baffle had a width of 220 mm. The casting procedure followed the Bridgman processes. Firstly, we melted the alloy in a crucible positioned in the induction melting coil. Then, we mounted the

investment mold cluster onto the chill plate and raised it into the mold-heater. A vacuum of 3×10^{-4} mbar was achieved in the furnace chamber before preheating the mold. The casting temperature was 1550 °C. After equalizing the mold temperature, the melted alloy was poured into the mold, and then the withdrawal sequence was initiated with a speed of 3 mm/min. Then, the single-crystal castings were formed.

Table 1. The analyzed chemical composition of the CM247LC alloy.

Element	Cr	Co	Mo	W	Al	Ta	Ti	C	Hf	Ni
Mass (wt.%)	8.2	9.2	0.5	9.4	5.6	3.2	0.7	0.08	1.1	Bal.

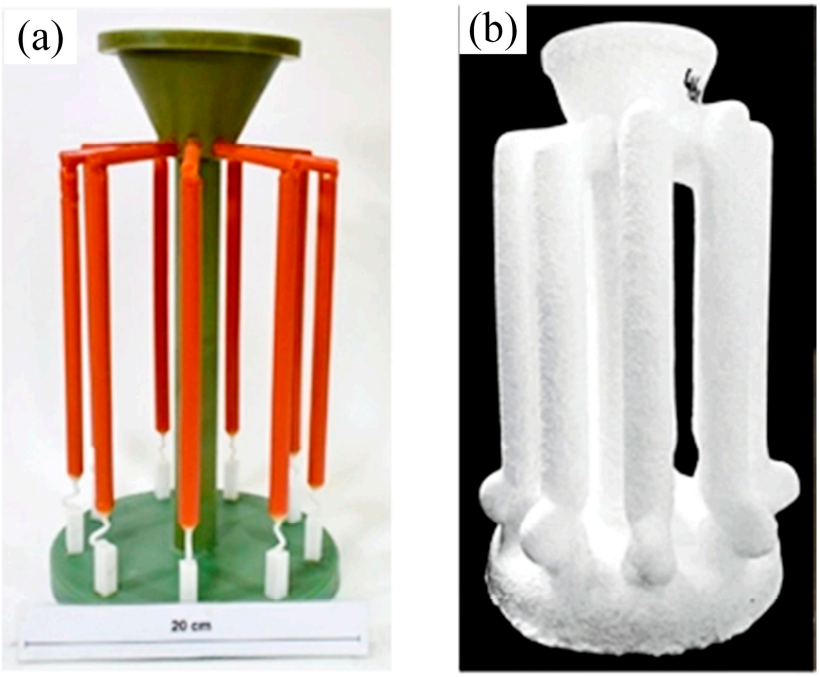


Figure 1. (**a**) Wax model. (**b**) The cluster of the ceramic shell.

All samples were prepared from the same casting with the same solidification conditions. After removing the ceramic debris, the castings were etched to reveal the macrostructure using a 50% H_2O_2 + 50% HCl etchant. Samples used for microstructural characterization were longitudinally cut from the selector parts. Samples were mounted in conductive phenolic powder and polished using a combination of grinding papers, ranging from 300 to 1000 grit, and then by diamond-based polishing solutions, ranging from 9 µm to 0.05 µm. Thereafter, a 60 mL C_2H_5OH + 40 mL HCl + 2 g $CuCl_2 \cdot 2H_2O$ etchant was used to show grain structure. The morphology and microstructure of the defects were observed using optical microscope (OM, Axio Observer, Carl Zeiss AG, Oberkochen, Germany) and electron back scatter diffraction(EBSDZeiss Sigma300, Carl Zeiss AG, Oberkochen, Germany).

In the C-shaped grain selector, as shown in Figure 2, the selector portion was designed with varying wire diameters (2.6–6.6 mm) and pitch lengths fixed at 8 mm. Table 2 summarize all the C-shaped grain selector samples.

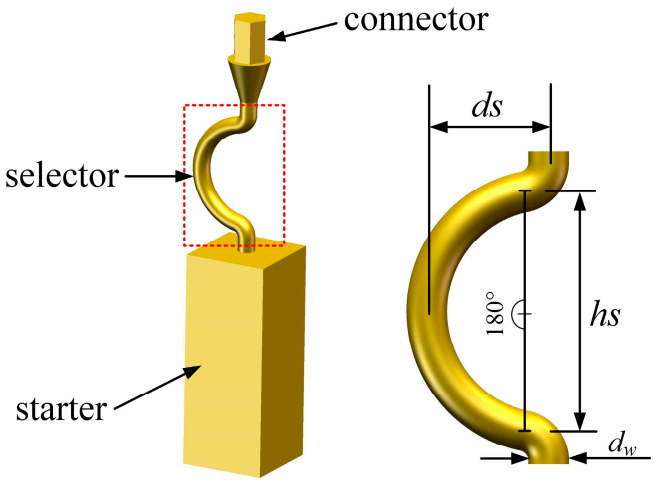


Figure 2. Schematic illustrations of the C-shaped grain selector.

Table 2. SCd-form grain selectors with different wire diameters.

Probe	SC_{d1}	SC_{d2}	SC_{d3}	SC_{d4}	SC_{d5}	SC_{d6}	SC_{d7}	SC_{d8}
Diameter (mm)	2.6	3.0	3.4	3.8	4.2	5.4	6.0	6.6
Pitch Length (mm)	8							
Selector Height (mm)	10							
Starter Block Size(mm)	10 (L) × 10 (W) × 30 (H)							

2.1.2. Experimental Results

The C-shaped grain selector parts with different wire diameters (2.6–6.6 mm) were cut after directional solidification, as shown in Figure 3. It can be seen that the slivers were mainly observed in the grain selection part. From the experiment results, it can be seen that the smaller wire diameter then the better the geometry block efficiency. From the SC_{d1} casting sample, it can be seen that the sliver was found, illuminating that the too-narrow wire diameter was not suitable. This result showed that the sliver formation was not caused by failure of the grain selection. Theoretically, the geometric constraints of grain selection imply that the ultra-fine grain selection channel should improve the efficiency of grain selection. Therefore, it could be speculated that the emergence of the sliver is not due to a failure in grain selection but rather due to a torsion caused by excessive stress concentration.

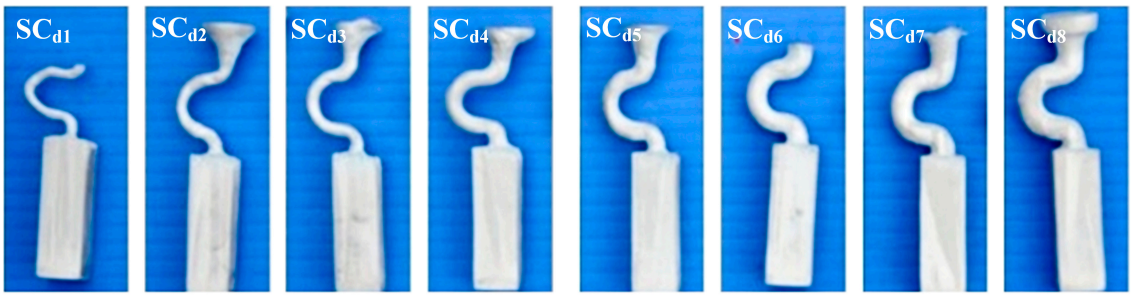


Figure 3. The C form grain selector with different wire diameters.

2.2. Numeral Simulation

In the grain selection process, the continuous bifurcation of dendrites in the grain selection channel leads to changes in the orientation of grains during the dendrite growth process, causing the orientation dispersion of grains. Therefore, it is difficult to determine the grain distribution and orientation in the analysis of microstructure evolution of directional solidification using EBSD and OM methods. Moreover, it is difficult to track the

competitive growth of grain, which brings trouble to the research results and analysis. However, in the numerical simulation process, the orientation of the grains did not change with the solidification process, and the orientation dispersion of the grains was not caused. Therefore, the tracking view of grain structure during directional solidification can be realized effectively via numerical simulation. In addition, conducting a large number of experimental studies increased production cost. Using numerical simulation can save a lot of time and cost before casting; it can also provide a theoretical basis for the analysis. Therefore, it is important to study the microstructure evolution of the directional solidification process using the simulation method.

As such, we first present the calculation model of the temperature field in the directional solidification process. A commercially available simulation software package (ProCAST, v 2021.5, ESI Group, Rungis, France) was used to simulate and analyze the temperature and stress field in the directional solidification process of the CM247LC alloy combined with the actual casting conditions. Finally, the calculation model of microstructure was described and analyzed.

2.2.1. Temperature Field Model

Generally, it is difficult to observe the formation of orientation defects and the evolution of the dendrite structure during the directional solidification of a single-crystal superalloy in real-time. However, numerical simulation technology can provide helpful information, such as the evolution of the temperature field during solidification. It can also significantly reduce the time and experimental cost required to optimize the solidification process. Therefore, in this study, the casting simulation software ProCAST was used to analyze the temperature field evolution and temperature gradient during the preparation of single-crystal superalloy blades.

The inner chamber of a directional solidification furnace can be divided into three distinct sections: the heating zone, the thermal baffle, and the cooling zone. The heat transfer involved in the directional solidification process is as follows: heat exchange between the solidified metal, the mold shell, and the chilling plate; heat conduction between the turbine blade and the mold shell; heat exchange between the turbine blade and the mold shell; heat radiation among the outer surface of the shell, the radiant baffle, and the inner wall of the furnace. The process can be divided into two types: heat conduction and heat radiation.

During the initial condition settings, the temperature of the upper and lower heating bodies is brought to the predetermined temperature, and the temperatures of the upper and lower surfaces of the chilling plate, the radiation baffle, and the inner furnace wall in the cooling zone are all set to constant values.

The thermophysical characteristics and boundary conditions are as follows:

(1) Heat conduction equation can be described as follows [23]:

$$\rho C_p \frac{\partial T}{\partial t} = \frac{\partial}{\partial x}\left(\lambda \frac{\partial T}{\partial x}\right) + \frac{\partial}{\partial y}\left(\lambda \frac{\partial T}{\partial y}\right) + \frac{\partial}{\partial z}\left(\lambda \frac{\partial T}{\partial z}\right) + \rho L_f \frac{\partial f_s}{\partial T} \quad (1)$$

where ρ is the alloy density, C_P is the heat capacity of the alloy, λ is the thermal conductivity, T is the temperature, t is time, L_f is the latent heat of crystallization, and f_S is the volume fraction of solid phase. The first item on the right side of the above formula is the heat conduction item. The second item is the internal heat source caused by the latent heat of crystallization.

(2) The heat radiation between the ceramic shell and furnace chamber is in accordance with the Stefan–Boltzmann law, which is described as follows [24]:

$$q = \varepsilon \sigma_0 T_s^4 \quad (2)$$

where the ε is radiation temperature, σ_0 is Stefan–Boltzmann constant, and T_s is the absolute temperature of the surface.

2.2.2. Mathematical Model of Stress Field

The shell is made of ceramic material with elastic material characteristics, following Hooke's law [25]:

$$\sigma = E\varepsilon \tag{3}$$

where σ is the stress, E is elastic coefficient, and ε is the strain.

The elastoplastic material constitutive model is used for the CM247LC superalloy. The force exerted on the primary dendrite is as follows [26]:

$$\sigma_{1\max} = \frac{4\rho u^2 d_1 H_B^2}{\pi d_1'^2} \cdot \cos^2(\theta) \tag{4}$$

The force exerted on a second dendrite is as follows:

$$\sigma_{2\max} = \frac{\rho u^2 d_2 \lambda_2^2}{\pi d_2'^2} \cdot \sin^2(\theta) \tag{5}$$

The yield strength near the melting point is as follows [27]:

$$\sigma_s(T) = 10^{-3} \cdot E(T) = 10^{-3}\left(1 + B \cdot \left(\frac{T-300}{T-T_m}\right)\right) \tag{6}$$

To avoid the primary dendrite yielding [28]:

$$\theta_1 < \arccos\left(\frac{10^{-3}\left(1 + B \cdot \left(\frac{T-300}{T-T_m}\right)\right)\pi d_1'^2}{\rho u^2 d_1 H_B^2}\right) \tag{7}$$

To avoid the second dendrite yielding:

$$\theta_2 < \arcsin\left(\frac{10^{-3}\left(1 + B \cdot \left(\frac{T-300}{T-T_m}\right)\right)\pi d_2'^2}{\rho u^2 d_2 \lambda_1^2}\right) \tag{8}$$

where ρ is the alloy density, σ is stress, σ_s is the yield strength, ε is strain, E is the elastic modulus of the material, u is Poisson's ratio, d_1 is diameter of the primary dendrite, d_1' is the mean diameter of the primary dendrite, d_2 is diameter of the secondary dendrites, d_2' is the mean diameter of the secondary dendrites, λ_1 is primary dendrite spacing, λ_2 is secondary dendrite spacing, θ is the deviation angle, B is fluid particle, T is temperature, T_m is melting temperature, and H_B is Herschel–Bulkley model, which is a model that lies between the Bingham model and the Ostwald–de Waele model [29]. It assumes that the stress–strain relationship of the fluid is linear below a certain stress threshold, and that nonlinear shear deformation occurs when the stress exceeds this threshold.

It can be seen from Equations (7) and (8) that the roots of the secondary branches are more prone to yielding behavior due to the solute enrichment in the necking zone, which means that in the overly narrow solidification zone that second dendrite more easily meets the yielding condition and torsion occurs first.

2.2.3. Simulation Parameters

The ProCAST software was used to simulate the temperature and stress field of the blade during the solidification stage. Grid division of the module was carried out. The grid size was set to 0.3 mm. The size of the grid determines the amount of data and the length of the running time. The setting of 0.3 mm of fast running time was deemed adequate for grain selection simulation without affecting the final casting dimensional accuracy. The number of grids was about 800,000. The physical parameters of materials are shown is Table 3. The casting temperature of the blade was 1550 °C. Therefore, the interface heat transfer coefficient between the superalloy and ceramic material was 750 W/(m^2·K), and

the heat transfer coefficient between the metal and chill plate was 3010 W/(m^2·K), as shown in Table 4.

Table 3. Physical parameters of the materials.

Temperature T (°C)	Density of Metal ρ_{Metal} (kg·m^{-3})	Thermal Conductivity λ_{Metal} (W·m^{-1}·°C^{-1})	Enthalpy of Metal E_M (kJ·Kg^{-1})
25	8.164	10.3	−368.7
400	8.016	15.3	191.1
1000	7.766	23.8	159.4
1324	7.505	32.8	450.1
1371	7.169	30.5	700.9
1550	7.016	33.4	837.3

Table 4. Interface heat-transfer coefficients.

Temperature T (°C)	Interface Heat-Transfer Coefficients $h_{Metal/Mold}$ (W·m^{-2}·°C^{-1})	Interface Heat-Transfer Coefficients $h_{Metal/Chill}$ (W·m^{-2}·°C^{-1})
25	150	80
400	150	600
1000	190	1510
1324	350	2000
1371	750	2250
1550	750	3010

3. Results and Discussion

3.1. Microscopic Morphology Analysis of Sliver Defects

Figure 4 shows the morphology of the sliver. The results indicate that the flaws are brilliant linear defects with divergent morphology, and the defect width increases with increasing height. Based on the size and location of the sliver, the source point was seen to be primarily located at the C-shaped grain selection. Subsequent findings revealed that the alteration position began at the junction between the top of the start block and the grain selection channel. The length of sliver in the grain selection was about 1 mm, and then quickly spread to more than 20 mm after entering the blade.

Furthermore, the sliver defect area of the blade was detached, and the sample was prepared for analysis via microscopic morphology. On the surface of sliver, the irregular metallographic structure boundary around the sliver indicated that it formed at the end of solidification, and the stress stretching occurred when there was still a small amount of liquid metal between the dendrites.

3.2. Solidification Interval of Superalloy

A DSC analyzer (404F3, NETZSCH-Gerätebau GmbH., Selb, Germany) was used for thermal analysis. Using the thermodynamic calculation software Thermo-calc (v2023a, Thermo-Calc Software, Stockholm, Sweden.), the relevant relationship between the solid-phase ratio and temperature was also determined. The test region and outcomes are depicted in Figure 5. The liquidus and solidus temperatures of CM247LC were calculated using the software PANDAT (v7.0, CompuTherm LLC, Middleton, WI, USA); the result is shown in Figure 5a. Figure 5b shows the differential scanning calorimetry (DSC) heating curves of CM247LC tested at the rate of 10 °C/min.

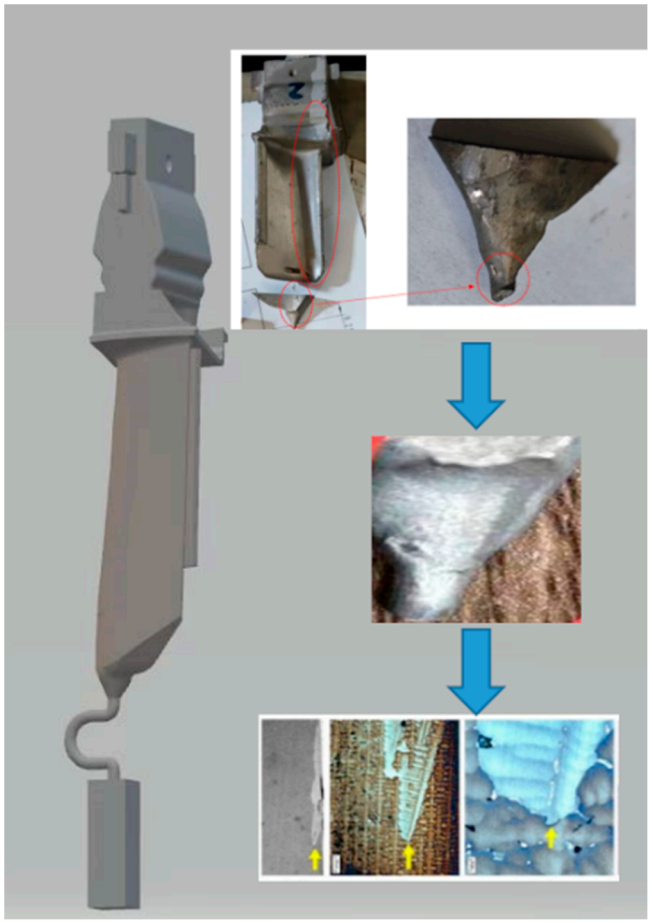


Figure 4. Illustration of the origin of sliver formation.

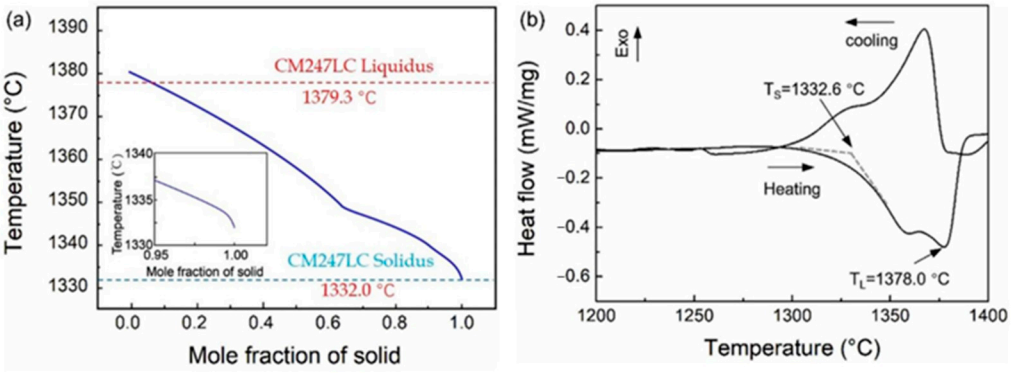


Figure 5. (**a**) Calculated mass fraction of equilibrium phases, and (**b**) the DSC heating curve of CM247LC.

It can be seen that the liquidus–solidus temperature of CM247LC ranged from 1332.0 °C to 1379.3 °C, as shown in Figure 5a. There is a large endothermic appears at 1332.6 °C that keeps increasing until 1378.0 °C, representing the TS and TL, respectively, as shown in Figure 5b. As a result, it was clear that the DSC result of CM247LC is in agreement with the simulation of PANDAT. As the temperature increases in the heating process, a significant endothermic peak appeared at 1332.6 °C and reached its maximum point at 1378 °C, which was assumed to indicate the continuing melting of the matrix phase. During the cooling phase, the sample exhibited a significant exothermic peak at 1365 °C, which was interpreted as a considerable volume of solidification and crystallization. In

addition, the sample exhibited exothermic peaks at 1257.3 °C, which can be interpreted as the solidification of the eutectic portion and the precipitation of the γ′ phase.

According to the analysis solidification behavior of CM247LC superalloy, the solidification temperature range was relatively wide. There was a low melting point phase with a low-volume fraction for a long time at the end of solidification, and the low melting point phase was determined to be a eutectic structure. Therefore, it can be inferred that the sliver defect formed in the solidification stage, especially at the end of solidification.

3.3. Numerical Calculation of Temperature Field

Since the sliver formed during the solidification interval, the temperature and stress fields during the solidification process were carefully investigated. It can be observed that as solidification advances, the rate of cooling gradually decreases. From the perspective of the solidification sequence, the sliver dendrites first solidified at the intersection of the crystal initiating section and the grain selection section. The solidification sequence was observed from bottom-to-top and from the mold shell wall toward the grain selection channel. The final solidification area was observed to be the middle of the grain selection channel.

Furthermore, due to the uniform wall thickness of the blade body, the temperature difference remained minimal within a particular range, resulting in a small temperature gradient in the direction of the blade height. Moreover, the temperature gradient was deemed significant because the start block section and the grain selection section were located at the abruptly changing section. At this point, there was not enough feeding, and it was easy for macroscopic shrinkage porosity or shrinkage cavity defects to emerge.

It can be seen from Figure 6 that with the progressing of solidification, the spacing between isotherms gradually increased, and the width of the mush zone rapidly widened. The shape of the temperature field and the isotherm under different diameters was almost the same, indicating that the wire diameter had little effect on the temperature field. The simulation results indicated that the temperature field had no direct influence on the formation of the sliver and that the formation was independent of the liquidus and solidus phase temperature change.

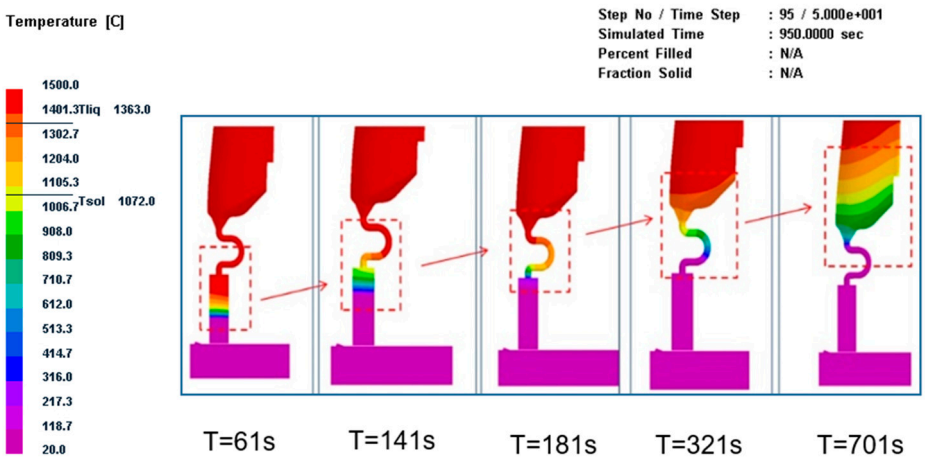


Figure 6. Evolution of the temperature field in a 2D grain selector.

3.4. Numerical Calculation of Stress Field

A numerical stress analysis was performed on the crystal starting section and abruptly changing section of the selected segment to explain the effects of stress on the sliver formation, as depicted in Figure 7. The results showed that the stress value always remains positive in the range of 0% to 100% in the solid fraction. This indicates that the selected point remained under continuous tensile stress during solidification. It also showed that as the solidification advanced, the tensile stress increased until it reached a peak value of about 25 MPa. At this point, the solid-phase ratio was 100%. The trajectory of the

curve revealed that the stress increased significantly between 80% and 100% in the solid fraction, demonstrating that the stress increased quickly at the end of solidification. It can be deduced that the cumulative tensile stress is more significant if the solid-phase ratio remains between 80% and 100% for an extended period of time. This finding provides proof of the rationale that a longer solidification interval will result in a more significant accumulated tensile stress at the end of solidification.

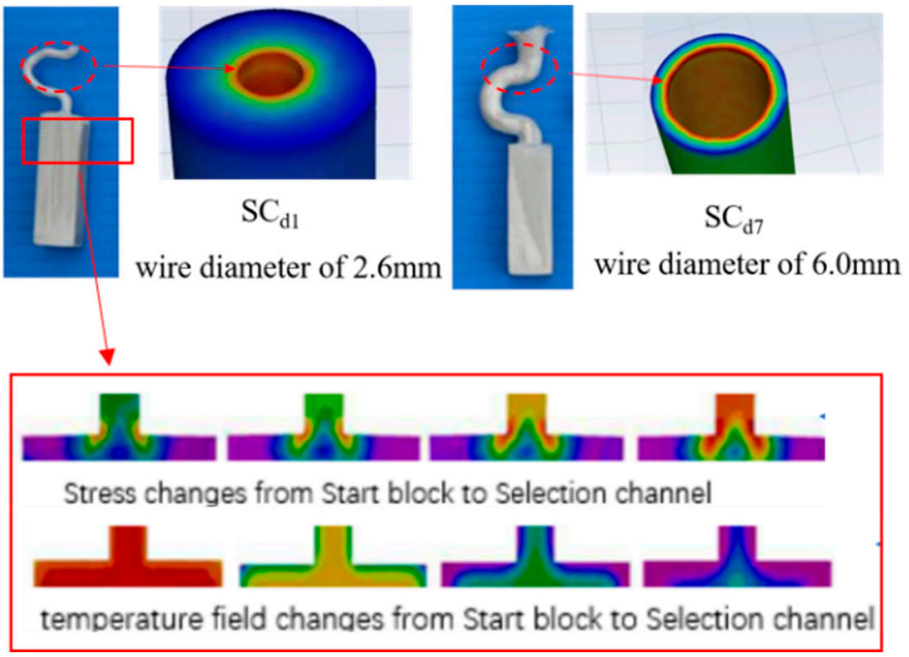


Figure 7. Stress distribution comparison between crystal separation channels with a wire diameter of 2.6 mm and 6 mm.

The horizontal stress in the grain selection channel was nearly the same. However, the number of grains through the grain selection channel with a wire diameter of 2.6 mm was only one-sixth of that obtained through the grain selection channel with a wire diameter of 6 mm. As a result, the stress on every single grain in the selection channel was six-times that in the 6-mm channel, which was more likely to cause twisting or breaking of longitudinal dendrites, resulting in the sliver formation.

Stress is concentrated if the grain selecting section is too narrow. Using a diameter of 2.6 mm as an example, only three-to-five grains can travel through the dendrites in this area. Consequently, a single dendrite of this area has more than 10-times the stress concentration of the start blocker and upper sample section. Because the cross-section of the upper blade segment and the lower crystal section is relatively large, the stress of a single dendrite under the same amount of stress is relatively small, and it is not easy to twist and stress extrusion.

As shown in Figure 8, the sliver occurred in the necking channel. It can be deduced that when the solid-phase isotherm passes through the necking channel, stress gathers in the channel, and when the stress value is greater than the yield strength of superalloy near the solid phase line, dendrite deflection occurs in the necking channel, resulting in the appearance of striations. At the same time, when this region is solidified, the yield strength of dendrites varies from softening to solid-phase formation during the solidification process. Equation (6) shows that the yield strength close to the melting point is related to the temperature field in the area during solidification. The inner core of the selection section is the last portion to solidify, and while the middle portion is still there, the portion closest to the shell solidifies fastest to produce a solid phase. Dendrites created

during the softening stage have very low yield strengths and are easily bent and twisted due to the surrounding stress brought on by softening.

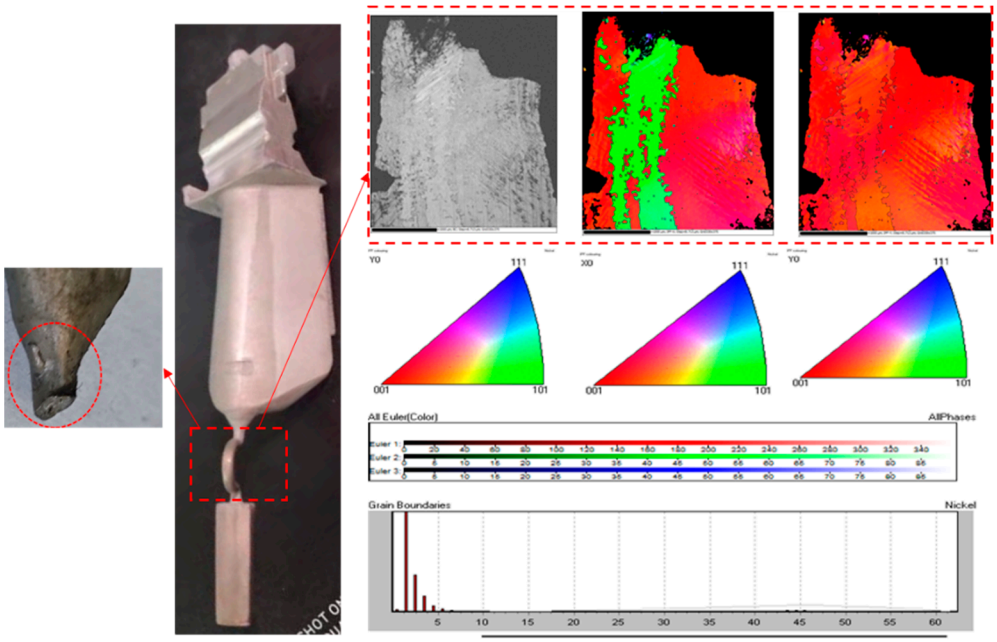


Figure 8. The illustration of longitudinal dendrites of the sliver in the necking channel of sample SC_{d2}.

3.5. Analysis of the Sliver Formation Mechanism

Figure 9a shows that the borders inside the single crystal are exceedingly irregular. The curved boundary is a grain boundary with a high angle that goes through the whole interior of the single crystal. Figure 9b shows that the curved grain boundary separates the single crystal into three regions. Among these, the left-and-right orientation regions are almost identical, but the orientation of the region having a curved grain boundary in the middle differs significantly from the overall single crystal orientation. Figure 9c shows that the interior of the single crystal has a higher local misorientation near the left and right borders, indicating that this region may have undergone a severe plastic deformation process. Figure 9d shows the distribution results of adjacent misorientation sections distributed horizontally across the single crystal. The results show that the misorientation size on both sides of the curved grain boundary within the single crystal is 43°, indicating a lager-angle grain boundary. This finding is consistent with the observations in the inverse pole figure. It is also noted that in other regions, the intra-grain orientations are all smaller than 5°, indicating that only small angle grain boundaries exist. Figure 9d shows the cumulative orientation difference distribution diagram. On the right side of Figure 9d, it can be observed that the grain orientation difference gradually increases from left to right in the single crystal region, and the intra-grain orientation difference as a whole can reach more than 10°, indicating a strong plastic deformation feature. The polarographic results of the single crystal shown in Figure 9e indicate that the orientation of the left-and-right parts of the single crystal is nearly identical. In contrast, the orientation of the single crystal with a solid curved grain boundary in the middle is significantly different from the parent orientation, but its square (100) is nearly identical.

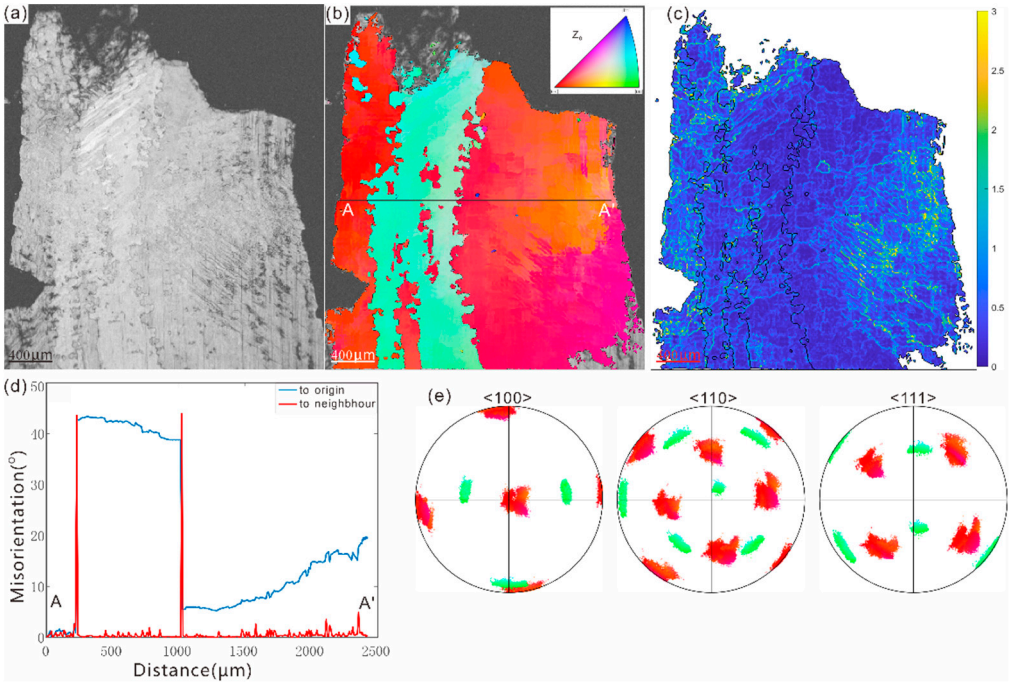


Figure 9. Twisting diagram of longitudinal dendrites of sliver in sample SC_d2. (**a**) The comparison between pattern quality; (**b**) the orientation of a single crystal. Color is drawn according to the reverse polar diagram of a single crystal along the direction of Z0. The background displays the pattern-quality image. (**c**) The difference in the local orientation, and the maximum difference in the local orientation is set at 3°. (**d**) The misorientation profile. The starting point represents point A, and the endpoint is representative of point A′ in (**b**). The red and blue lines represent adjacent misorientation and cumulative misorientation, respectively. (**e**) Diagram showing the polar image of a single crystal particle, and the lower hemisphere is projected using an equal-area projection method.

Therefore, according to the analysis of the microstructure, solidification interval, temperature, and stress fields of the sliver defect during investment casting of single-crystal superalloy with the C-shaped 2D grain selectors, the formation mechanism of the sliver can be revealed as follows:

1. The sliver formation initiates at the points that undergo an abrupt transformation, especially at the junction of crystal initiation and separation segments, where the temperature gradient is significant, and the solidification rate is slow.
2. The sliver forms among primary dendrites, where many eutectic structures with low melting points are easily formed.
3. The sliver mainly forms at the end of solidification. At this point, the liquid phase's volume fraction is minimal, and it is not easy to replenish the solidification shrinkage with the remaining liquid metal. In addition, the stress grows with the progression of solidification, and the accumulated stress reaches its maximum value at the end of solidification.
4. The region with the sliver defect experiences significant tensile stress. The casting exhibits volume changes during solidification due to the lengthy solidification interval of the casting superalloy, which could cause the emergence of many eutectic phases with low melting points among the dendrites at the end of solidification. The dendrites are displaced due to the action of tensile stress and cannot be replenished by the liquid phase, which allows for the formation of the sliver.

4. Conclusions

In this study, we investigated the effects of the C-shaped 2D grain selectors on the solidification behavior of a superalloy and a sliver formation mechanism. The following conclusions were drawn: The sliver forms in the final stages of solidification and especially originates in the grain selection part where the accumulated thermal stress is high, and there is only a small quantity of liquid phase with a low melting point between the dendrites. At this point, the solidification and stress conditions generate thermal cracks. The sliver forms at the corner of the abruptly changing section, where the solidification rate is slow, but the temperature gradient and thermal stress are large. Alloy composition and solidification interval properties provide the basis for the formation of the sliver. Furthermore, the restraint state and tensile stress on the dendrite boundary are the main causes for the formation and expansion of the slivers.

Author Contributions: Q.Y.: writing—original draft, investigation, funding acquisition, and writing—review and editing; X.Z.: data curation, formal analysis, investigation, and writing—original draft; F.W.: methodology, supervision, and funding acquisition; D.M.: conceptualization, validation, data curation, and investigation. J.W.: methodology and validation. All authors have read and agreed to the published version of the manuscript.

Funding: This work was supported by the Natural Science Basic Research Plan in Shaanxi Province of China (Grant No.2022JQ-553), the National Science and Technology Major Project (No. HT-J2019-VI-0020-0136), China Postdoctoral Science Foundation (Grant NO. 2021M692555), and the Excellent Youth Foundation of Shaanxi Province of China (No. 2021JC-08).

Data Availability Statement: The raw/processed data required to reproduce these findings cannot be shared at this time as the data also forms part of an ongoing study.

Acknowledgments: The authors acknowledge the National Youth Talent Support Program and the Youth Innovation Team of Shaanxi Universities.

Conflicts of Interest: The authors declare that they have no known competing financial interests or personal relationships that could have appeared to influence the work reported in this paper.

References

1. Xia, W.; Zhao, X.; Yue, L.; Zhang, Z. Microstructural evolution and creep mechanisms in Ni-based single crystal superalloys: A review. *J. Alloys Compd.* **2020**, *819*, 152954. [CrossRef]
2. Ding, Q.; Bei, H.; Yao, X.; Zhao, X.; Wei, X.; Wang, J.; Zhang, Z. Temperature effects on deformation substructures and mechanisms of a Ni-based single crystal superalloy. *Appl. Mater. Today* **2021**, *23*, 101061. [CrossRef]
3. Dai, H.J.; Gebelin, J.C.; D'Souza, N.; Brown, P.D.; Dong, H. Effect of spiral shape on grain selection during casting of single crystal turbine blades. *Int. J. Cast Met. Res.* **2009**, *22*, 54–57. [CrossRef]
4. Meng, X.; Li, J.; Jin, T.; Sun, X.; Sun, C.; Hu, Z. Evolution of grain selection in spiral selector during directional solidification of nickel-base superalloys. *J. Mater. Sci. Technol.* **2011**, *27*, 118–126. [CrossRef]
5. Gheisari, H.; Karamian, E. Characterization and investigation of grain selection in spiral grain selectors during casting single-crystal turbine blades. *J. Mod. Process. Manuf. Prod.* **2015**, *4*, 19–28.
6. Dai, H.; D'souza, N.; Dong, H.B. Grain selection in spiral selectors during investment casting of single-crystal turbine blades: Part I. Experimental investigation. *Metall. Mater. Trans. A* **2011**, *42*, 3430–3438. [CrossRef]
7. Zhu, X.; Wang, F.; Ma, D.; Bührig-Polaczek, A. Grain selection in a high-efficiency 2D grain selector during casting of single-crystal superalloys. *Materials* **2019**, *12*, 789. [CrossRef]
8. Zhu, X.; Wang, F.; Ma, D.; Bührig-Polaczek, A. Development of a high-efficiency z-form selector for single crystal blades and corresponding grain selection mechanism. *Materials* **2019**, *12*, 780. [CrossRef]
9. Zhu, X.; Yang, Q.; Wang, F.; Ma, D. Grain orientation optimization of two-dimensional grain selector during directional solidification of Ni-based superalloys. *Materials* **2020**, *13*, 1121. [CrossRef]
10. Xu, W.; Wang, F.; Ma, D.; Zhu, X.; Li, D.; Bührig-Polaczek, A. Sliver defect formation in single crystal Ni-based superalloy castings. *Mater. Des.* **2020**, *196*, 109138. [CrossRef]
11. Xia, H.; Yang, Y.; Feng, Q.; Xu, Q.; Dong, H.; Liu, B. Generation mechanism and motion behavior of sliver defect in single crystal Ni-based superalloy. *J. Mater. Sci. Technol.* **2023**, *137*, 232–246. [CrossRef]
12. Beech, J.; Jones, H. *Solidification Processing 1997: Proceedings of the 4th Decennial International Conference on Solidification Processing*; University of Sheffield: Sheffield, UK, 1997; pp. 33–41.

13. Napolitano, R.E.; Schaefer, R.J. The convergence-fault mechanism for low-angle boundary formation in single-crystal castings. *J. Mater. Sci.* **2000**, *35*, 1641–1659. [CrossRef]
14. Aveson, J.; Tennant, P.; Foss, B.; Shollock, B.; Stone, H.; D'Souza, N. On the origin of sliver defects in single crystal investment castings. *Acta Mater.* **2013**, *61*, 5162–5171. [CrossRef]
15. Huang, Y.; Shen, J.; Wang, D.; Xie, G.; Lu, Y.; Lou, L.; Zhang, J. Formation of sliver defect in Ni-based single crystal superalloy. *Metall. Mater. Trans. A* **2020**, *51*, 99–103. [CrossRef]
16. Huang, Y.; Shen, J.; Wang, D.; Xie, G.; Lu, Y.; Lou, L.; Zhang, J. Evolution of sliver defect in Ni-based single crystal superalloy. *Metall. Mater. Trans. A* **2020**, *51*, 6364–6372. [CrossRef]
17. Huo, M.; Liu, L.; Yang, W.; Sun, D.; Hu, S.; Zhang, J.; Fu, H. Formation of Slivers in the Extended Cross-Section Platforms of Ni-Based Single Crystal Superalloy. *Adv. Eng. Mater.* **2018**, *20*, 1701189. [CrossRef]
18. Sun, D.; Liu, L.; Huang, T.; Yang, W.; He, C.; Li, Z.; Zhang, J.; Fu, H. Formation of lateral sliver defects in the platform region of single-crystal superalloy turbine blades. *Metall. Mater. Trans. A* **2019**, *50*, 1119–1124. [CrossRef]
19. Han, D.; Jiang, W.; Xiao, J.; Li, K.; Lu, Y.; Lou, L. Investigating the evolution of freckles into sliver defects in Ni-based single-crystal superalloy castings. *Mater. Today Commun.* **2021**, *27*, 102350. [CrossRef]
20. Ma, D.; Wang, F.; Xu, W.; Zhu, X.; Li, D.; Bührig-Polaczek, A. Formation of Sliver Defects in Single CrystalCastings of Superalloys. *Acta Met. Sin.* **2019**, *56*, 301–310.
21. Pilling, J.; Hellawell, A. Communications: Mechanical Deformation of Dendrites by Fluid Flow. *Metall. Mater. Trans. A* **1996**, *27*, 229–232. [CrossRef]
22. Dragnevski, K.; Mullis, A.M.; Walker, D.J.; Cochrane, R.F. Mechanical deformation of dendrites by fluid flow during the solidification of undercooled melts. *Acta Mater.* **2002**, *50*, 3743–3755. [CrossRef]
23. Zhang, H.; Xu, Q. Simulation and experimental studies on grain selection and structure design of the spiral selector for casting single crystal Ni-based superalloy. *Materials* **2017**, *10*, 1236. [CrossRef]
24. Zhang, H.; Xu, Q. Multi-scale simulation of directional dendrites growth in superalloys. *J. Mater. Process. Technol.* **2016**, *238*, 132–141. [CrossRef]
25. Yan, X.; Guo, X.; Liu, Y.-L.; Gong, X.-F.; Xu, Q.-Y.; Liu, B.-C. Numerical simulation of dendrite growth in Ni-based superalloy casting during directional solidification process. *Trans. Nonferrous Met. Soc. China* **2019**, *29*, 338–348. [CrossRef]
26. Dahle, A.; John, D.H.S.; Thevik, H.J.; Arnberg, L. Modeling the fluid-flow-induced stress and collapse in a dendritic network. *Metall. Mater. Trans. B* **1999**, *30*, 287–293. [CrossRef]
27. Keller, T.; Lindwall, G.; Ghosh, S.; Ma, L.; Lane, B.M.; Zhang, F.; Kattner, U.R.; Lass, E.A.; Heigel, J.C.; Idell, Y.; et al. Application of finite element, phase-field, and CALPHAD-based methods to additive manufacturing of Ni-based superalloys. *Acta Mater.* **2017**, *139*, 244–253. [CrossRef]
28. Huang, W.; Li, S.; Yang, X.; Shi, D.; Qi, H. Experimental investigation and modelling of microstructure degradation in a DS Ni-based superalloy using a quantitative cross-correlation analysis method. *J. Alloys Compd.* **2018**, *762*, 488–499. [CrossRef]
29. Divoux, T.; Barentin, C.; Manneville, S. From stress-induced fluidization processes to Herschel-Bulkley behaviour in simple yield stress fluids. *Soft Matter* **2011**, *7*, 8409–8418. [CrossRef]

Disclaimer/Publisher's Note: The statements, opinions and data contained in all publications are solely those of the individual author(s) and contributor(s) and not of MDPI and/or the editor(s). MDPI and/or the editor(s) disclaim responsibility for any injury to people or property resulting from any ideas, methods, instructions or products referred to in the content.